*Sensors and Materials*, Vol. 37, No. 3 (2025) 1181–1192
MYU Tokyo 

S & M 3980

# Speed Estimation Rotor-flux-vector-controlled Induction Motor Drive Based on Adaptive Flux Estimator

Yung-Chang Luo,* Wei-Chen Lin, Hao-You Huang, and Wen-Cheng Pu

Department of Electrical Engineering, National Chin-Yi University of Technology,
No. 57, Sec. 2, Zhongshan Rd, Taiping Dist, Taichung 41170, Taiwan (ROC)

(Received June 27, 2024; accepted February 6, 2025)

***Keywords:*** rotor flux vector control (RFVC), speed estimation, flux estimator, model reference adaptive control (MRAC), ant colony optimization (ACO) algorithm

A speed estimation scheme was proposed for the rotor-flux-vector-controlled (RFVC) induction motor (IM) drive. The decoupled RFVC IM drive was developed on the basis of stator current and rotor flux, with the measured stator current obtained from the IM using Hall effect current sensors. A model reference adaptive control rotor flux estimator was designed, utilizing both voltage-model and current-model rotor fluxes, and the adaptation mechanism was optimized using the ant colony optimization algorithm. The estimated rotor speed was derived from the adaptive rotor flux estimator. The MATLAB®/Simulink toolbox was employed to simulate this system, and all control algorithms were implemented on a TI DSP 6713 and F2812 microcontrol card to validate the proposed approach. Both simulation and experimental results confirmed the effectiveness of the method.

## 1. Introduction

Induction motors (IMs) are commonly used in hostile environments owing to their inherent robustness, low maintenance requirements, and cost-effectiveness. The mathematical model of an IM is time-varying, coupled, and nonlinear, making it more complex to achieve precise and high-performance motor control compared with other types of motor. By applying the flux vector control (FVC) method, similar to that used in a separately excited DC motor, the torque and flux can be independently controlled. According to the FVC theory,[1] through coordinate transformation, the complex mathematical model of an IM can be decomposed into torque-current and flux-current components. Since torque and flux are orthogonal to each other, the maximum torque-to-current ratio can be achieved. Generally, the motor drive maintains the rated flux and operates in the constant torque mode below the base speed. Above the base speed, the flux setting decreases as speed increases, operating in the constant power mode. In conventional rotor FVC (RFVC) IM drives, an encoder is typically required to detect the shaft position. However, this sensor degrades drive robustness and is unsuitable for hostile environments. Various speed prediction methods for RFVC IM drives have been published,

*Corresponding author: e-mail: luoyc@ncut.edu.tw
https://doi.org/10.18494/SAM5219

including speed determination by an observer or a flux estimator,(2–7) speed identification using fuzzy logic control or neural networks,(8–12) speed estimation using the extended Kalman filter,(13–16) and speed adjustment based on the adaptive control theory.(17–20) In this research, a decoupled RFVC IM drive was established on the basis of the stator current and rotor flux, with three-phase stator current measurements conducted using electromagnetic Hall effect current sensors. According to the model reference adaptive control (MRAC) theory, a rotor flux estimator was developed using both voltage-model and current-model rotor fluxes, with the estimated speed derived from this rotor flux estimator. The adaptation mechanism of the MRAC rotor flux estimator was designed using the ant colony optimization (ACO) algorithm. These approaches confirmed the successful implementation of a promising speed estimation RFVC IM drive using the adaptive rotor flux estimator.

This paper is organized into six sections. In Sect. 1, we present the research background and motivation and review the literature on speed estimation methods for RFVC IM drives. In Sect. 2, we describe the decoupled RFVC IM drive system. The development of the speed estimation scheme based on the MRAC rotor flux estimator is detailed in Sect. 3. In Sect. 4, we explain the adaptation mechanism design using the ACO algorithm. In Sects. 5 and 6, we discuss the simulation and experimental results, followed by the conclusions.

## 2. Decoupled RFVC IM Drive

The stator and rotor voltage equations of an IM in the synchronous reference frame are given as(21)

$$R_s\vec{i}_s^{\,e} + j\omega_e\vec{\lambda}_s^e + p\vec{\lambda}_s^e = \vec{v}_s^{\,e}, \tag{1}$$

$$R_r\vec{i}_r^{\,e} + j\omega_{sl}\vec{\lambda}_r^e + p\vec{\lambda}_r^e = 0, \tag{2}$$

where $j$ represents the imaginary part; $\vec{i}_s^{\,e} = i_{ds}^e + ji_{qs}^e$ and $\vec{v}_s^{\,e} = v_{ds}^e + jv_{qs}^e$ denote the stator current and voltage, $\vec{\lambda}_s^e = \lambda_{ds}^e + j\lambda_{qs}^e$ and $\vec{\lambda}_r^e = \lambda_{dr}^e + j\lambda_{qr}^e$ are the stator and rotor fluxes, and $R_s$ and $R_r$ are the stator and rotor resistances, respectively; $\vec{i}_r^{\,e} = i_{dr}^e + ji_{qr}^e$ is the rotor current; $\omega_e$ is the speed of the synchronous reference frame; $\omega_{sl} = \omega_e - \omega_r$ is the slip speed; $\omega_r$ is the electrical speed of the rotor; and $p = d/dt$ is the differential operator.

The stator and rotor fluxes are defined as

$$\vec{\lambda}_s^e = L_s\vec{i}_s^{\,e} + L_m\vec{i}_r^{\,e}, \tag{3}$$

$$\vec{\lambda}_r^e = L_m\vec{i}_s^{\,e} + L_r\vec{i}_r^{\,e}, \tag{4}$$

where $L_s$ and $L_r$ represent the stator and rotor inductances, respectively, and $L_m$ denotes the mutual inductance between the stator and the rotor.

Under a RFVC condition ($\lambda_{qr}^e = 0$), the $d^e$-axis estimated rotor flux and estimated slip speed are respectively derived as

$$\hat{\lambda}_{dr}^{e} = \frac{L_m i_{ds}^{e}}{1+\tau_r s}, \tag{5}$$

$$\hat{\omega}_{sl} = \frac{L_m i_{qs}^{e}}{\tau_r \lambda_{dr}^{e}}, \tag{6}$$

where the symbol ^ denotes the estimated value, $\tau_r = L_r / R_r$ is the rotor time constant, and $s$ is the Laplace operator.

The developed electromagnetic torque under the RFVC condition is derived as

$$T_e = \frac{3P}{4} \cdot \frac{L_m}{L_r} \cdot i_{qs}^{e} \hat{\lambda}_{dr}^{e}, \tag{7}$$

where $P$ is the number of motor poles. Since $i_{qs}^{e}$ and $\hat{\lambda}_{dr}^{e}$ are orthogonal and can be independently controlled, the maximum torque-to-current ratio is achieved.

The mechanical equation of an IM is given by

$$B_m \omega_{rm} + J_m p \omega_{rm} = T_e - T_L, \tag{8}$$

where $B_m$ is the viscous friction coefficient, $J_m$ is the inertia of the IM, $T_L$ is the load torque, and $\omega_{rm} = (2/P)\omega_r$ is the mechanical speed of the motor shaft.

Under the RFVC condition, with Eqs. (3) and (4), the state matrix of an IM is derived from Eqs. (1) and (2) as

$$p\begin{bmatrix} i_{ds}^{e} \\ i_{qs}^{e} \\ \hat{\lambda}_{dr}^{e} \end{bmatrix} = \begin{bmatrix} -\frac{R_s}{\sigma L_s} - \frac{1-\sigma}{\sigma \tau_r} & \omega_e & \frac{1-\sigma}{\sigma L_m \tau_r} \\ -\omega_e & -\frac{R_s}{\sigma L_s} & -\frac{1-\sigma}{\sigma L_m}\omega_e \\ \frac{L_m}{\tau_r} & 0 & -\frac{1}{\tau_r} \end{bmatrix} \begin{bmatrix} i_{ds}^{e} \\ i_{qs}^{e} \\ \hat{\lambda}_{dr}^{e} \end{bmatrix} + \begin{bmatrix} \frac{1}{\sigma L_s} v_{ds}^{e} \\ \frac{1}{\sigma L_s} v_{qs}^{e} \\ 0 \end{bmatrix}, \tag{9}$$

where $\sigma = 1 - L_m^2 / L_s L_r$ is the leakage inductance coefficient.

In Eq. (9), an inspection of the right side of the first row reveals that the second and third terms are coupling components related to $i_{qs}^{e}$ and $\hat{\lambda}_{dr}^{e}$, respectively. Similarly, an inspection of the right side of the second row shows that the first and third terms are coupling components related to $i_{ds}^{e}$ and $\hat{\lambda}_{dr}^{e}$, respectively. On the basis of these coupling components, the $d^e$-axis and $q^e$-axis stator voltage feed-forward compensations are given by

$$v_{ds\_fc}^{e} = -\omega_e i_{qs}^{e} - \frac{1-\sigma}{\sigma L_m \tau_r} \hat{\lambda}_{dr}^{e}, \tag{10}$$

$$v_{qs\_fc}^{e} = \omega_e i_{ds}^{e} + \frac{1-\sigma}{\sigma L_m}\omega_e \hat{\lambda}_{dr}^{e}. \tag{11}$$

Thus, the linear relationship of $d^e$-axis and $q^e$-axis stator current control loops is achieved.

The voltage commands for the $d^e$-axis and $q^e$-axis stator current control loops are respectively given by

$$v_{ds}^{e^*} = \left(1/\left(\sigma L_s\right)\right)v_{ds}^{e'} + v_{ds\_fc}^{e}, \tag{12}$$

$$v_{qs}^{e^*} = \left(1/\left(\sigma L_s\right)\right)v_{qs}^{e'} + v_{qs\_fc}^{e}. \tag{13}$$

Here, $v_{ds}^{e'}$ and $v_{qs}^{e'}$ are the outputs of the $d^e$-axis and $q^e$-axis stator current controllers, respectively. The decoupled linear state matrix of an IM is given by

$$p\begin{bmatrix} i_{ds}^{e} \\ i_{qs}^{e} \\ \hat{\lambda}_{dr}^{e} \end{bmatrix} = \begin{bmatrix} -\frac{R_s}{\sigma L_s} - \frac{1-\sigma}{\sigma\tau_r} & 0 & 0 \\ 0 & -\frac{R_s}{\sigma L_s} & 0 \\ 0 & 0 & -\frac{1}{\tau_r} \end{bmatrix}\begin{bmatrix} i_{ds}^{e} \\ i_{qs}^{e} \\ \hat{\lambda}_{dr}^{e} \end{bmatrix} + \begin{bmatrix} v_{ds}^{e^*} \\ v_{qs}^{e^*} \\ \frac{L_m}{\tau_r} i_{ds}^{e} \end{bmatrix}. \tag{14}$$

According to the first, second, and third rows of Eq. (14), the plant models for the $d^e$-axis and $q^e$-axis stator current control loops and the flux control loop are respectively derived as

$$G_{P\_i_{ds}^{e}}(s) = 1/\left(s + R_s/\sigma L_s + (1-\sigma)/\sigma\tau_r\right), \tag{15}$$

$$G_{P\_i_{qs}^{e}}(s) = 1/\left(s + R_s/\sigma L_s\right), \tag{16}$$

$$G_{P\_\lambda_{dr}^{e}}(s) = \left(L_m/\tau_r\right)/\left(s + 1/\tau_r\right). \tag{17}$$

The plant of the speed control loop is derived from Eq. (8) as

$$G_{P\_\omega_{rm}}(s) = \left(1/J_m\right)/\left(s + B_m/J_m\right). \tag{18}$$

The decoupled linear control block diagram of the RFVC IM drive is shown in Fig. 1. Here, ($K_{ps}$, $K_{is}$), ($K_{pf}$, $K_{if}$), ($K_{pd}$, $K_{id}$), and ($K_{pq}$, $K_{iq}$) are the proportional and integral gain parameter pairs for the speed, flux, $d^e$-axis, and $q^e$-axis stator current controllers, respectively. The control

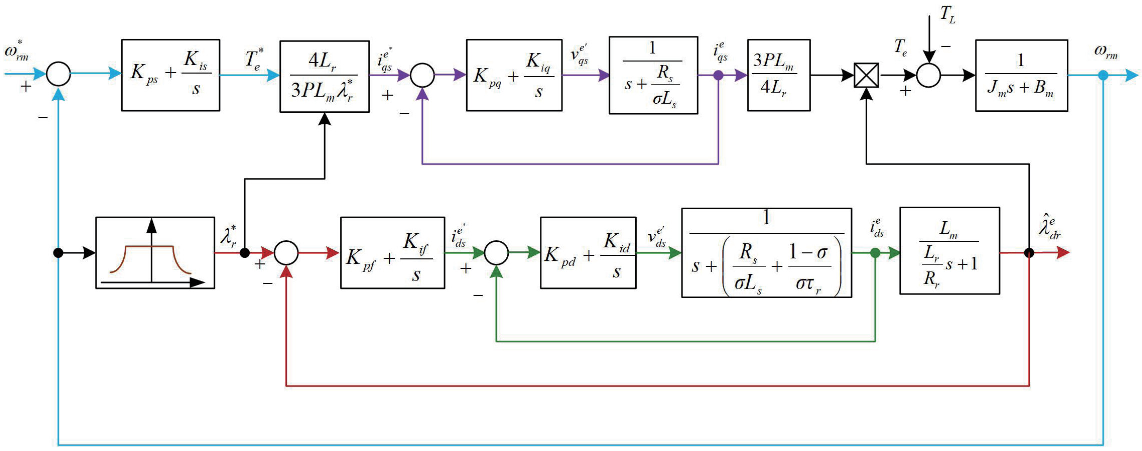


Fig. 1. (Color online) Decoupled linear control block diagram of RFVC IM drive.

gain of the internal control loop is much higher than that of the external control loop, allowing the closed-loop gain of the internal control loop to be regarded as unity. Therefore, Eqs. (17) and (18) are selected as the plant models for the flux and speed control loops, respectively.

## 3. Speed Estimation Based on MRAC Rotor Flux Estimator

The speed estimation RFVC IM drive requires an estimated rotor speed signal instead of the feedback rotor speed used in a convectional RFVC IM drive. In this research, the estimated rotor speed is derived from the MRAC rotor flux estimator.

In the stationary reference coordinate frame ($\omega_e = 0$), the current-model rotor flux estimator is derived from Eqs. (2) and (4) as

$$p\hat{\vec{\lambda}}_{ri}^{s} = \left(L_m / \tau_r\right)\vec{i}_s^{s} - \left(1/\tau_r - j\hat{\omega}_r\right)\hat{\vec{\lambda}}_{ri}^{s}, \tag{19}$$

where $\hat{\vec{\lambda}}_{ri}^{s} = \hat{\lambda}_{dri}^{s} + j\hat{\lambda}_{qri}^{s}$. The voltage-model rotor flux estimator is derived from Eqs. (1), (3), and (4) as

$$p\hat{\vec{\lambda}}_{rv}^{s} = \left(L_r / L_m\right)\left(\vec{v}_s^{s} - (R_s + \sigma L_s p)\vec{i}_s^{s}\right), \tag{20}$$

where $\hat{\vec{\lambda}}_{rv}^{s} = \hat{\lambda}_{drv}^{s} + j\hat{\lambda}_{qrv}^{s}$. According to the MRAC theory,[22] the voltage-model rotor flux estimator without the estimated rotor speed ($\hat{\omega}_r$) is selected as the reference model, while the current-model rotor flux estimator containing $\hat{\omega}_r$ is selected as the adjustable model. The difference between the reference and adjustable models is given by

$$\varepsilon = \hat{\lambda}_{dri}^{s}\hat{\lambda}_{qrv}^{s} - \hat{\lambda}_{qri}^{s}\hat{\lambda}_{drv}^{s}. \tag{21}$$

The MRAC rotor flux estimator is illustrated in Fig. 2. Here, the difference ($\varepsilon$) is passed through an adaptation mechanism to obtain the estimated rotor speed.

## 4. Adaptation Mechanism Design Using ACO Algorithm

The ACO algorithm was employed to design the adaptation mechanism of the MRAC rotor flux estimator due to its robustness, parallel processing capability, and effective global search abilities. The ACO algorithm, inspired by the foraging behavior of ants in the biological world, is a simulated evolutionary algorithm.[23] Ants use group cooperation to find food, secreting pheromones to mark favorable paths. These pheromones attract more ants to follow the same path, which ultimately accelerates the search and leads to the discovery of the global optimal solution. The ACO algorithm naturally supports parallel processing, as each ant searches independently without the need for global message synchronization, facilitating distributed computing. The ACO algorithm comprises two main components: the transition rule and the pheromone update rule.[24]

(A) Transition rule: the probability of an ant moving from position $i$ to position $j$ is given by

$$p_{ij}(t) = \frac{[\tau_{ij}(t)]^{\alpha}[\eta_{ij}(t)]^{\beta}}{\sum[\tau_{ij}(t)]^{\alpha}[\eta_{ij}(t)]^{\beta}}, \tag{22}$$

where $\tau_{ij}$ represents the pheromone concentration on path $ij$, $\alpha$ is the control influence coefficient for $\tau_{ij}$, $\eta_{ij}$ is the initial value of pheromones on path $ij$, and $\beta$ is the control influence coefficient for $\eta_{ij}$.

(B) Pheromone update rule:

$$\tau_{ij}(t+1) = (1-\rho)\tau_{ij}(t) + \Delta\tau_{ij}(t), \tag{23}$$

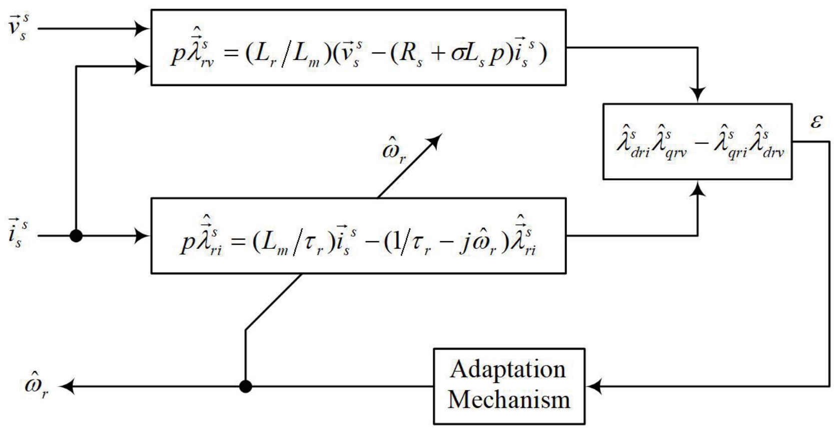


Fig. 2. Block diagram of MRAC rotor flux estimator.

where $\rho$ is the pheromone evaporation rate, with $0 < \rho \leq 1$; $\Delta\tau_{ij}$ represents the pheromones deposited by ants and $\Delta\tau_{ij}$ is defined as

$$\Delta\tau_{ij}(t) = \beta / L_k, \tag{24}$$

where $\beta$ is a constant and $L_k$ represents the travel length of the $k$-th ant.

Figure 3 illustrates the flow chart of the proposed ACO algorithm adaptation mechanism design.

Figure 4 shows the block diagram of the proposed speed estimation RFVC IM drive based on the MRAC rotor flux estimator. This diagram includes a speed controller, a flux controller, $d^e$-axis and $q^e$-axis stator current controllers, $d^e$-axis and $q^e$-axis decoupling calculations, a speed-based flux command, $i_{qs}^{e*}$-calculation, coordinate transformations between the three-phase system and the two-axis stationary reference frame ($2^s \Leftarrow 3$, $2^s \Rightarrow 3$), coordinate transformations between the two-axis synchronous reference frame and the two-axis stationary reference frame ( $2^e \Rightarrow 2^s$, $2^e \Leftarrow 2^s$), and the MRAC rotor flux estimator. In this system, the speed controller, flux controller, and $d^e$-axis and $q^e$-axis stator current controllers were designed using root locus and Bode plot techniques. The adaptation mechanism for the MRAC rotor flux estimator was developed using the ACO algorithm. Furthermore, the three-phase currents ($i_{as}$, $i_{bs}$, and $i_{cs}$) were obtained from the IM using electromagnetic Hall effect current sensors.

## 5. Simulation Setup and Results

A three-phase, 220 V, 0.75 kW, Δ-connected standard squirrel cage IM was used as the controlled plant for experimentation to confirm the effectiveness of the proposed speed

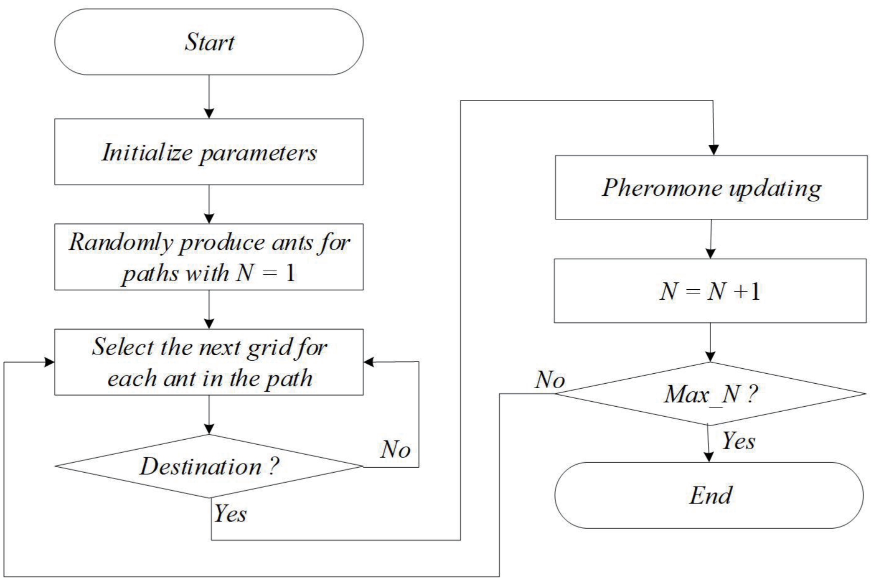


Fig. 3. Flow chart of proposed ACO algorithm adaptation mechanism design.

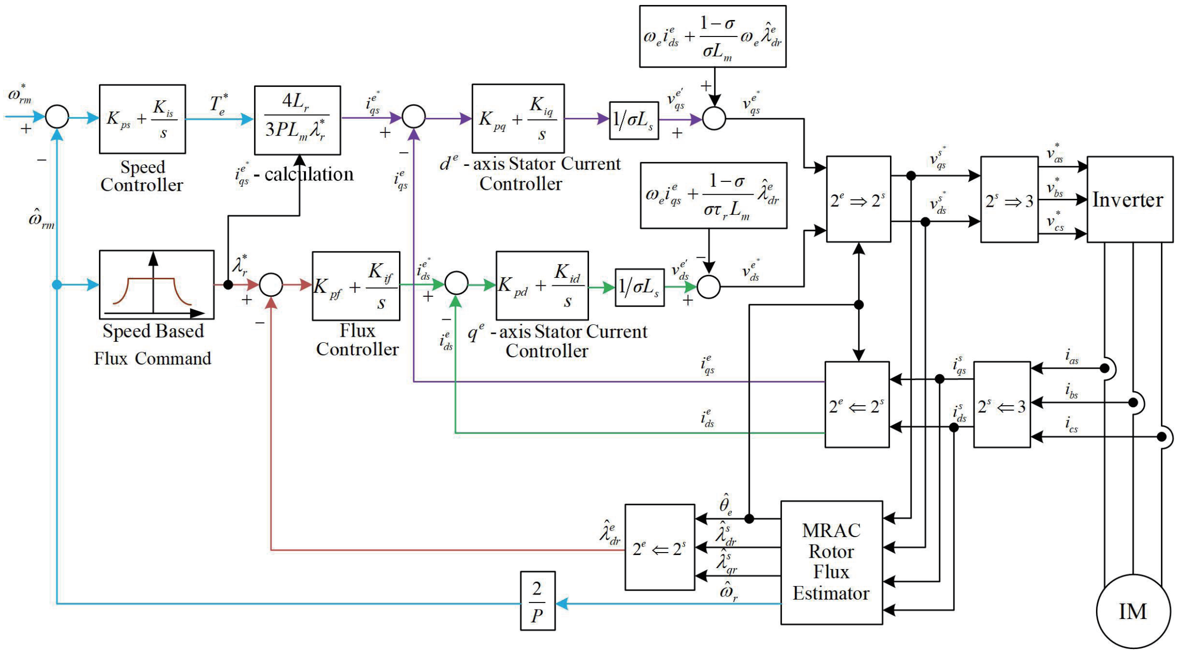


Fig. 4. (Color online) Block diagram of speed estimation RFVC IM drive based on MRAC rotor flux estimator.

estimation RFVC IM drive based on the MRAC rotor flux estimator. The speed command in a running cycle was designed as follows: forward acceleration from $t$ = 0 to $t$ = 1 s, forward steady-state running over $1 \leq t \leq 2$ s, forward braking to reach zero speed within the interval $2 \leq t \leq 3$ s, reverse acceleration from $t$ = 3 to $t$ = 4 s, reverse steady-state running over $4 \leq t \leq 5$ s, and reverse braking to reach zero speed within the interval $5 \leq t \leq 6$ s.

The simulated and experimental responses of the proposed speed estimation RFVC IM drive based on the MRAC rotor flux estimator in both constant torque and constant power modes are shown in Figs. 5 and 6, and Figs. 7 and 8, respectively. Each figure presents six responses: (a) command (dashed line) and estimated (solid line) rotor speed, (b) command (dashed line) and actual (solid line) rotor speed, (c) $q^e$-axis stator current, (d) electromagnetic torque, (e) estimated synchronous position angle, and (f) estimated rotor flux locus. The simulated and experimental responses under a 2 N-m load for reversible steady-state speed commands of 1200 and 2400 rev/min are also shown in Figs. 5 and 6, and Figs. 7 and 8, respectively. Notably, the estimated rotor flux locus in constant power mode is smaller than that in constant torque mode.

On the basis of the simulated and experimental responses observed in different reversible transient and steady-state operations, the MRAC rotor flux estimator with the ACO adaptation mechanism accurately estimates rotor speeds in both constant torque and constant power modes. The $q^e$-axis stator current and electromagnetic torque responses confirm the loading effect. The sawtooth pattern of the estimated synchronous position angle and the circular shape of the estimated rotor flux locus verify the accuracy of the coordinate transformation between the synchronous and stationary reference frames. Therefore, the developed speed estimation RFVC IM drive based on the MRAC rotor flux estimator has demonstrated that the desired performance can be achieved.

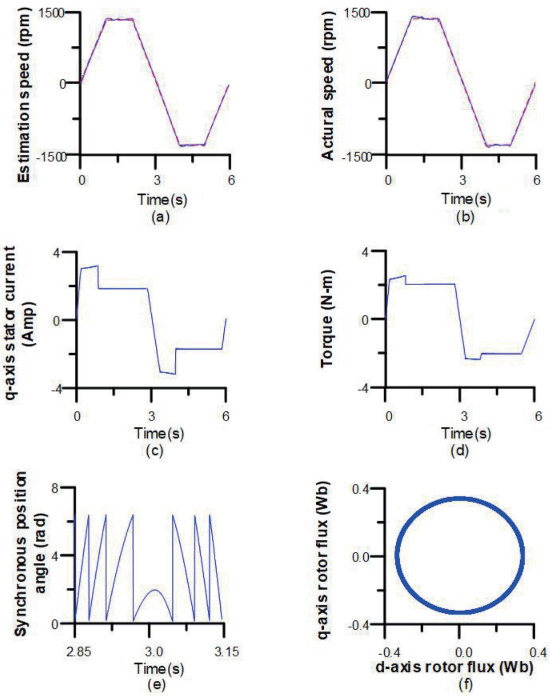


Fig. 5. (Color online) Simulated responses of the proposed speed estimation RFVC IM drive based on the MRAC rotor flux estimator with a 2 N-m load for a reversible steady-state speed command of 1200 rev/min: (a) estimated rotor speed, (b) actual rotor speed, (c) $q^e$-axis stator current, (d) electromagnetic torque, (e) estimated synchronous position angle, and (f) estimated rotor flux locus ($q^e$-axis vs $d^e$-axis).

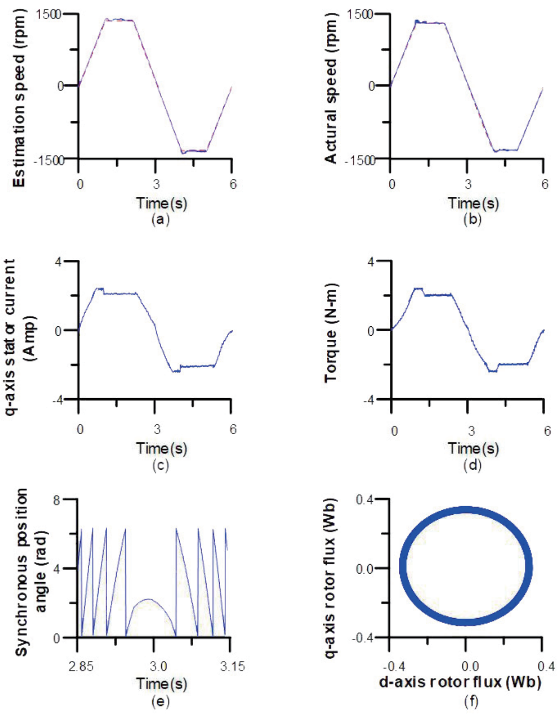


Fig. 6. (Color online) Experimental responses of the proposed speed estimation RFVC IM drive based on the MRAC rotor flux estimator with a 2 N-m load for a reversible steady-state speed command of 1200 rev/min: (a) estimated rotor speed, (b) actual rotor speed, (c) $q^e$-axis stator current, (d) electromagnetic torque, (e) estimated synchronous position angle, and (f) estimated rotor flux locus ($q^e$-axis vs $d^e$-axis).

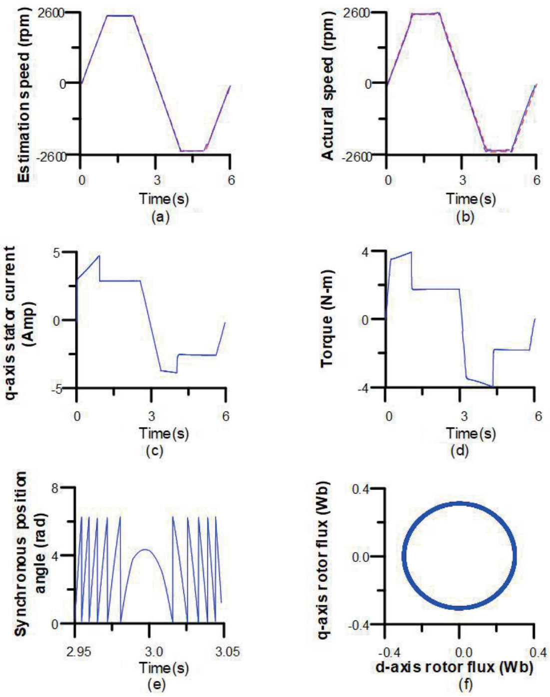


Fig. 7. (Color online) Simulated responses of the proposed speed estimation RFVC IM drive based on the MRAC rotor flux estimator with a 2 N-m load for a reversible steady-state speed command of 2400 rev/min: (a) estimated rotor speed, (b) actual rotor speed, (c) $q^e$-axis stator current, (d) electromagnetic torque, (e) estimated synchronous position angle, and (f) estimated rotor flux locus ($q^e$-axis vs $d^e$-axis).

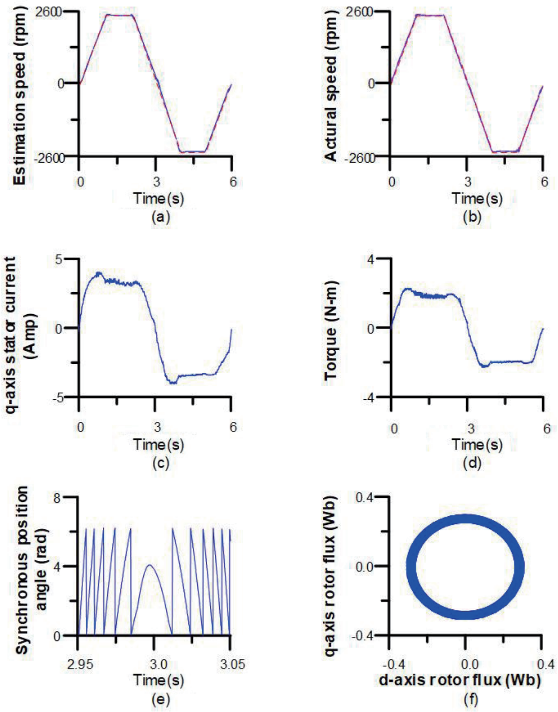


Fig. 8. (Color online) Experimental responses of the proposed speed estimation RFVC IM drive based on the MRAC rotor flux estimator with a 2 N-m load for a reversible steady-state speed command of 2400 rev/min: (a) estimated rotor speed, (b) actual rotor speed, (c) $q^e$-axis stator current, (d) electromagnetic torque, (e) estimated synchronous position angle, and (f) estimated rotor flux locus ($q^e$-axis vs $d^e$-axis).

## 6. Conclusions

An MRAC rotor flux estimator was developed for the speed estimation RFVC IM drive. The decoupled RFVC IM drive was established on the basis of the stator current and rotor flux. Speed estimation was derived from the MRAC rotor flux estimator using both the voltage-model- and current-model-estimated rotor fluxes, with the adaptation mechanism designed using the ACO algorithm. The three-phase stator current measurements required for implementing the speed estimation RFVC IM drive were conducted using Hall effect current sensors. Simulation and experimental responses for reversible steady-state speed commands under a load condition in both constant torque and constant power modes confirmed the promising performance of the proposed speed estimation RFVC IM drive based on the MRAC rotor flux estimator.

## Acknowledgments

This study was supported by the National Science and Technology Council of Taiwan under contract number NSTC 111-2637-E-167-004 (duration: August 1, 2022–July 31, 2023).

## References

1 Y. C. Luo, B. W. Chen, W. C. Pu, and N. S. Pai: Sens. Mater. **32** (2020) 239. https://doi.org/10.18494/SAM.2020.2574
2 H. Chen, J. Li, Y. Lu, K. Yang, L. Wu, and Z. Liu: IEEE Trans. Transp. Electrif. **10** (2024) 8. https://doi.org/10.1109/TTE.2023.3257056
3 J. Chen and J. Huang: IEEE Trans. Control Syst. Technol. **27** (2019) 2630. https://doi.org/10.1109/TCST.2018.2863668
4 T. Wang, B. Wang, Y. Yu, and D. Xu: IEEE Trans. Ind. Electron. **70** (2023) 11055. https://doi.org/10.1109/TIE.2022.3227272
5 G. J. Jo and J. W. Choi: IEEE Trans. Power Electron. **37** (2022) 4497. https://doi.org/10.1109/TPEL.2021.3126331
6 J. Chen and J. Huang: IEEE Trans. Power Electron. **34** (2019) 33. https://doi.org/10.1109/TPEL.2018.2836956
7 W. Sun, J. Gao, X. Liu, Y. Yu, G. Wang, and D. Xu: IEEE Trans. Ind. Appl. **52** (2016) 472. https://doi.org/10.1109/TIA.2015.2480852
8 A. V. R. Teja, V. Verma, and C. Chakraborty: IEEE Trans. Ind. Electron. **62** (2015) 6797. https://doi.org/10.1109/TIE.2015.2432105
9 M. K. Metwaly, N. I. Elkalashy, M. S. Zaky, and T. M. Wolbank: IEEE Trans. Energy Convers. **33** (2018) 68. https://doi.org/10.1109/TEC.2017.2726998
10 Y. Zhang, J. Zhu, Z. Zhao, W. Xu, and D. G. Dorrell: IEEE Trans. Power Electron. **27** (2012) 1502. https://doi.org/10.1109/TPEL.2010.2043543
11 S. M. Gadoue, D. Giaouris, and J. W. Finch: IEEE Trans. Energy Convers. **25** (2010) 394. https://doi.org/10.1109/TEC.2009.2036445
12 A. Nurettin and N. İnanç: IEEE J. Emerging Sel. Top. Power Electron. **11** (2023) 4332. https://doi.org/10.1109/JESTPE.2023.3265352
13 D. Pasqualotto, S. Rigon, and M. Zigliotto: IEEE Trans. Ind. Electron. **70** (2023) 1321. https://doi.org/10.1109/TIE.2022.3159962
14 Z. Yin, G. Li, Y. Zhang, and J. Liu: IEEE Trans. Ind. Inf. **15** (2019) 650. https://doi.org/10.1109/TII.2018.2810850
15 Md. Habibullah and D. D. C. Lu: IEEE Trans. Ind. Electron. **62** (2015) 6765. https://doi.org/10.1109/TIE.2015.2442525
16 I. M. Alsofyani, N. R. N. Idris, and K. B. Lee: IEEE Trans. Power Electron. **33** (2018) 7959. https://doi.org/10.1109/TPEL.2017.2773129
17 Y. Zuo, X. Ge, Y. Zheng, Y. Chen, H. Wang, and A. T. Woldegiorgis: IEEE Trans. Transp. Electrif. **8** (2022) 3336. https://doi.org/10.1109/TTE.2022.3148412

18 Y. B. Zbede, S. M. Gadoue, and D. J. Atkinson: IEEE Trans. Ind. Electron. **63** (2016) 3511. https://doi.org/10.1109/TIE.2016.2521721
19 H. Wang, Y. Zuo, Y. Zheng, C. Lin, X. Ge, X. Feng, Y. Yang, A. T. Woldegiorgis, D. Chen, and S. Li: IEEE Trans. Ind. Appl. **58** (2022) 2107. https://doi.org/10.1109/TIA.2022.3144964
20 H. Wang, Y. Yang, X. Ge, Y. Zuo, X. Feng, D. Chen, and Y. C. Liu: IEEE Trans. Ind. Electron. **70** (2023) 12168. https://doi.org/10.1109/TIE.2023.3239879
21 C. H. Liu: Control of AC Electrical Machines (Tunghua, Taipei, 2008) 4th ed., Chap. 6 (in Chinese).
22 A. N. Smith, S. M. Gadoue, and J. W. Finch: IEEE Trans. Energy Convers. **31** (2016) 270. https://doi.org/10.1109/TEC.2015.2480961
23 K. M. Sim and W. H. Sun: IEEE Trans. Syst. Man Cybern. Part A Syst. Humans **33** (2003) 560. https://doi.org/10.1109/TSMCA.2003.817391
24 H. C. Lu, H. K. Liu, and L. F. Yang: Proc. 2013 Int. System Science and Engineering Conf. (ICSSE, 2013) 319–324. https://doi.org/10.1109/ICSSE.2013.6614683